A Comparative Review of the Histogram-based Image Segmentation Methods

Zhenzhou Wang*

School of computer science and technology, Huaibei Normal University, Huaibei City, Anhui Province, China

*Corresponding author

E-mail: wangzz@chnu.edu.cn; 18553358239@, 163.com

Abstract

The histogram of an image is the accurate graphical representation of the numerical grayscale distribution and it is also an estimate of the probability distribution of image pixels. Therefore, histogram has been widely adopted to calculate the clustering means and partitioning thresholds for image segmentation. There have been many classical histogram-based image segmentation methods proposed and played important roles in both academics and industry. In this article, the histories and recent advances of the histogram-based image segmentation techniques are first reviewed and then they are divided into four categories: (1), the means-based method; (2), the Gaussianmixture-model-based method; (3), the entropy-based method and (4) the feature-points-based method. The principles of the classical histogram-based image segmentation methods are described at first and then their performances are compared objectively. In addition, the histogram-based image segmentation methods are compared with the general-purpose deep learning methods in segmenting objects with uniform or simple backgrounds. The histogram-based image segmentation methods are more accurate than the universal deeplearning methods without special training in segmenting many types of images.

Keywords: Histogram-based image segmentation; K-means; Fuzzy C-means; Expectation maximization; Entropy; Deep learning.

1. Introduction

Image segmentation divides a grayscale or color image into different meaningful regions and extracts the target objects, which plays an important role in many fields, such as real-time 3D measurement [1-3] and smart medical care [4-5]. Ever since 1960s, image segmentation studies have received significant attention from different researchers around the world and the histogram-based image segmentation methods have also made great progress in the following decades. For instance, the kmeans method [6] had been proposed in the 1960s and used for image segmentation [7] in the 1970s. Both the expectation maximization (EM) method [8] and the maximum inter-class difference method [9] were proposed for segmenting the grayscale images in the 1970s. The fuzzy C-means method [10], the maximum-entropy method [11-12], the cross-entropy method [13] and the feature-points-based method [14] were proposed for image segmentation in the 1980s. Due to the great variety of the images acquired in different application scenarios, the performances of these image segmentation methods usually lack stability. As a result, these methods were used directly in some applications or were optimized extensively by different researchers to improve their performances in other applications.

Based on the working principles, there are mainly four types of histogram-based image segmentation methods that fall into four categories. The first category is the means-based methods that include the k-means methods [15-23], the Otsu's method [24-33] and the fuzzy C-means methods [34-56]. The similarity of these methods is that all of them compute the class means iteratively. The differences of these methods are that the K-means method only calculates the class means in each iteration, the Otsu method calculates a proportion coefficient for each class mean, and the fuzzy C-means method calculates a fuzzy membership function for each class mean. Despite the straightforward working principles, researchers are still working on optimizing the performances of these methods nowadays. For instance, the normalized cross-correlation was used to improve the K-means clustering accuracy in [16] and better initialization algorithms were used to improve the Kmeans clustering accuracy in [17]. To optimize the performance of the Otsu's method, a support vector machine that is based on the Levy horse was proposed to compute multi-level thresholds optimally with significant improvement in [26]. In addition, the chameleon swarm algorithm was improved to increase the convergence of the Otsu's method in [31]. To improve the accuracy of the fuzzy C-means method, the gradient descent was used to solve an unconstrained fuzzy C-means algorithm and accordingly a novel deep fuzzy clustering model was obtained for clustering [39]. The second category is the Gaussian-mixture-model-based method that uses the EM methods [57-64] to calculate the mixture model's parameters. This category of method assumes that the histogram distribution consists of K Gaussian distributions and the histogram distribution could thus be denoted as a Gaussian distribution mixture model. The maximum A posteriori method [8], the least squared error method and the cross-correlation method could be used to generate the cost function for minimization by iteration. The iteration processes of the above three methods are the same, the iteration times are usually different and the accuracies vary insignificantly. The third category is the entropy-based methods that include the max Shannon entropy methods [65-66], the fuzzy Shannon entropy methods [67-70], the Shannon cross-entropy methods [71-78] and other entropy maximization methods [79-100]. The max Shannon entropy methods have been proved to be similar to the maximum-likelihood and Bayesian methods [11]. In histogrambased threshold selection, the max Shannon entropy method globally finds the thresholds that make the Shannon information entropy of all the independent pixel classes in the histogram distribution maximum. Similar to the max Shannon entropy method, the fuzzy Shannon entropy method also globally finds the thresholds that make the Shannon information entropy of all the independent pixel classes in the

histogram distribution maximum. Different from the max Shannon entropy method, the fuzzy entropy method adds a fuzzy membership function to its cost function. The cross Shannon entropy calculates the difference between two probability distributions. It had become a well-known concept of information theory for many decades and had been widely used in many different fields [13]. The cross Shannon entropy method uses the cross entropy distance or the metric cross entropy distance to define the cost function. Besides the Shannon entropy, the Renyi entropy [79-86], the Tsallis entropy [87-89], the Kapur entropy [90-93] and the Masi entropy [94-95] are also used for threshold selection. Similar to the max Shannon entropy method, these entropy-based methods also globally find the thresholds that make the information entropy of all the independent pixel classes in the histogram distribution maximum. The difference is that the entropy calculation formula is replaced accordingly. The fourth category is the feature-points-based method that uses the grayscale positions that generate the feature points with global or local maximum rates of change to calculate the clustering means or partitioning thresholds [101-107]. This category of method has been based on the assumption that the rate of change at the border of two pixel-classes in the histogram distribution will reach the global maximum or at least a local maximum and the rate of change at the center of a pixel-class will also reach the global maximum or at least a local maximum, which can be easily observed. In addition, the points with the global or local maximum rate of change can be treated as the histogram feature points. For instance, the representative histogram feature points are the histogram peaks and histogram valleys. Since the shape of the histogram could reflect the histogram feature points, this category of method is also called histogram-shape-based method in [108].

The universal bottleneck problem of these histogram-based methods described above is that they usually could not segment the objects under non-uniform or complex backgrounds robustly. Since the deep learning methods extract the objects based on their features instead of the gray levels, they could overcome this bottleneck problem potentially. As a result, deep learning has been paid a lot of attention in recent years and many large-scale annotation-based image datasets have emerged for training the deep neural networks. Although deep learning has made great achievements in image segmentation, it still has many challenges [109-116]. For instance, the annotations are usually sparse and limited. The classes are usually imbalanced. The overfitting problem and the gradient vanishing problem may exist. The training time is usually considerably long. Most importantly, it will be intractable for deep learning to predict the attention map at the pixel level. As a result, it usually requires post-processing algorithms, such as the conditional random filed [117] to optimize the predication results. In addition, some applications might have very limited resources for the deep learning training. At this time, the histogram-based image segmentation methods are usually preferred as a better choice. For the applications in which the images are suitable for both the deep learning based image segmentation methods and the histogram based image segmentation methods, the histogram based image segmentation methods are usually preferred as be a better

choice in the economic sense. Though many research efforts have been conducted to improve the histogram-based image segmentation methods in recent years, their limitations remain in segmenting the objects with non-uniform or complex backgrounds. Thus, the image segmentation methods based on the histograms and the image segmentation methods based on deep learning will be complementary in a long time.

The organization of this review is as follows. Firstly, the principles of the means-based methods that include the Kmeans method, the Otsu's method and the fuzzy C-means method are described. Secondly, the principles of the Gaussianmixture-model-based methods that include the maximum A posteriori method, the least squared error method and the crosscorrelation method are described. Thirdly, the principles of the entropy-based methods that include the maximum entropy method, the fuzzy entropy method and the cross-entropy method are described. Fourthly, the principles of the rate-ofchange-based methods that include the histogram-peak-and valley method and the slope-difference-distribution method are described. Fifthly, these described methods are evaluated and compared with the deep learning methods on the synthesized images. Sixthly, these described methods are evaluated and compared with the deep learning methods on the real images. At last, conclusions are drawn.

2. The Means-based Method

2.1 The K-means method

The popular K-means method [6-7] updates the means of the histogram iteratively to find the minimum of the summed squared errors between the clustered pixels and the means they belong to, which could be formulated as:

$$J^{2} = \sum_{i=1}^{T_{1}} (i - \mu_{1})^{2} + \sum_{k=2}^{K-1} \sum_{i=T_{k-1}+1}^{T_{k}} (i - \mu_{k})^{2} + \sum_{i=T_{k-1}+1}^{N} (i - \mu_{K})^{2}$$
 (1)

 μ_k represents the mean of the *k*th class and it is computed by the following equation.

$$\mu_{k} = \begin{cases} \sum_{i=1}^{T_{i}} \frac{i \times p(y_{i})}{T_{i}}; k = 1\\ \sum_{i=1}^{T_{k}} p(y_{i}) \end{cases}; k = 1\\ \sum_{i=T_{k-1}+1}^{T_{k}} \frac{i \times p(y_{i})}{\sum_{i=T_{k-1}+1}^{T_{k}} p(y_{i})}; k = 2, ..., K-1 \end{cases}$$

$$\sum_{i=T_{k-1}+1}^{N} \frac{i \times p(y_{i})}{\sum_{i=T_{k-1}+1}^{N} p(y_{i})}; k = K$$

$$(2)$$

In each iteration, the pixels are classified again based on their distances to the clustering center μ_k with the following equation.

$$\bar{k} = \underset{k=1,...,K}{\arg\min} |i - \mu_k|; i = 1, 2, ..., N$$
 (3)

k denotes the class number that the pixel i belongs to. Each pixel y_i will belong to one of the K pixel classes that are formulated as:

$$y_{i}^{k} = \begin{cases} [1,...,T_{1}]; k = 1\\ [T_{k-1} + 1,...,T_{k}]; k = 2,...,K-1\\ [T_{K-1} + 1,...,N]; k = K \end{cases}$$
(4)

With the newly determined pixel classes, μ_k are computed again by Eq. (2). The iteration stops until the cost function formulated by Eq. (1) converges, i.e.,

$$J^{n+1} - J^n < \Delta \tag{5}$$

where J^{n+1} denotes the cost function formulated by Eq. (1) in the next iteration and J^n denotes the cost function formulated by Eq. (1) in the current iteration. Δ denotes a predefined threshold. Or the means vector $(\mu_1, \mu_2, ..., \mu_K)$ converges, i.e.,

$$(\mu_1, \mu_2, ..., \mu_K)^{n+1} - (\mu_1, \mu_2, ..., \mu_K)^n < \Delta$$
 (6)

The thresholds could also be computed as follows.

$$T_k = \frac{\mu_k + \mu_{k+1}}{2}; k = 1, 2, ... K - 1$$
 (7)

2.2 The Otsu method

The famous Otsu method [9] globally or iteratively finds the means that maximize the differences between the interclasses in the histogram distribution, which can be formulated as follows.

$$J = \sqrt{\sum_{k=1}^{K} w_k \left(\mu - \mu_k\right)^2} \tag{8}$$

 μ denotes the mean of the whole histogram distribution and it is computed with the following equation.

$$\mu = \sum_{i=1}^{N} \frac{i \times p(y_i)}{\sum_{i=1}^{N} p(y_i)}$$
(9)

 w_k denotes the proportion of the kth class in the histogram distribution and it is computed with the following equation.

$$w_{k} = \begin{cases} \sum_{i=1}^{T_{i}} p(y_{i}); k = 1\\ \sum_{i=T_{k-1}+1}^{T_{k}} p(y_{i}); k = 2, ..., K-1\\ \sum_{i=T_{K-1}+1}^{N} p(y_{i}); k = K \end{cases}$$
(10)

 μ_k represents the mean of the kth class and it is computed by the following equation.

$$\mu_{k} = \begin{cases} \sum_{i=1}^{T_{i}} \frac{i \times p(y_{i})}{w_{1}}; k = 1\\ \sum_{i=T_{k-1}+1}^{T_{k}} \frac{i \times p(y_{i})}{w_{k}}; k = 2, ..., K-1\\ \sum_{i=T_{k-1}+1}^{N} \frac{i \times p(y_{i})}{w_{K}}; k = K \end{cases}$$
(11)

In each iteration, the pixels are classified again based on their distances to the clustering center μ_k with Eqs. (3-4). With the newly determined pixel classes, w_k and μ_k are computed again by Eq. (10) and Eq. (11) respectively. The iteration stops until the cost function formulated by Eq. (8) converges or the means vector $(\mu_1, \mu_2, ..., \mu_K)$ converges.

2.3 The fuzzy-C-means method

Like the K-means method, the popular fuzzy-C-means method [10] also updates the means of the histogram iteratively to find the minimum of the summed squared errors between the clustered pixels and the means they belong to. Different from the K-means method, it adds a fuzzy membership function to its cost function and it could be formulated as:

$$J^{2} = \sum_{i=1}^{T_{1}} u_{i1}^{m} (i - \mu_{1})^{2} + \sum_{k=2}^{C-1} \sum_{i=T_{k-1}+1}^{T_{k}} u_{ik}^{m} (i - \mu_{k})^{2} + \sum_{i=T_{k-1}+1}^{N} u_{iC}^{m} (i - \mu_{C})^{2}$$
(12)

 u_{ij} denotes the fuzzy membership function and it is computed with the following equation.

$$u_{ij} = \frac{1}{\left(x_i - \mu_j\right)^{\frac{2}{m-1}} \sum_{k=1}^{C} \left(\frac{1}{\left(x_i - \mu_k\right)^{\frac{2}{m-1}}}\right)}$$
(13)

 μ_j denotes the mean of the *j*th class in the histogram distribution and it is computed with the following equation.

$$\mu_{j} = \frac{\sum_{i=1}^{N} i \times u_{ij}^{m} \times p(y_{i})}{\sum_{i=1}^{N} u_{ij}^{m} \times p(y_{i})}; j = 1, ..., C$$
(14)

In each iteration, the fuzzy membership u_{ij} of each pixel is computed again with Eq. (13). With the newly computed fuzzy membership u_{ij} , μ_j is computed again by Eq. (14). The iteration stops until the cost function formulated by Eq. (12) converges or the means vector $(\mu_1, \mu_2, ..., \mu_C)$ converges. The thresholds are then computed by Eq. (7).

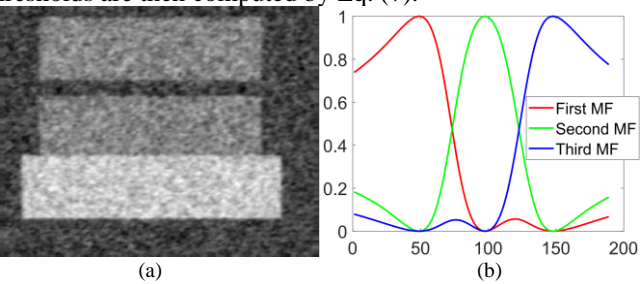


Fig. 1. Demonstration of the synthesized image and its computed fuzzy membership functions. (a) The synthesized image; (b) The computed fuzzy membership functions.

An image with three rectangles is synthesized by MATLAB as follows. The gray levels of the background belong to the first pixel class and are assigned as 100. The gray levels of the two smaller rectangles belong to the second pixel class and are assigned as 150. The gray levels of the largest rectangle belong

to the third pixel class and are assigned as 200. Then the Gaussian noises are added by multiplying the standard normal distribution with an amplitude 50. Fig. 1 (a) shows the synthesized image. The computed fuzzy membership functions (MF) by Eq. (13) for the first, second and third pixel class are demonstrated as the red, green and blue curve respectively. They are denoted as "First MF", "Second MF" and "Third MF" respectively in Fig. (b).

3. The Gaussian-mixture-model-based Method

This type of method assumes that the histogram distribution is composed of K Gaussian distributions and the histogram distribution could thus be denoted as a Gaussian distribution mixture model. Suppose the kth Gaussian distribution has the parameter that is denoted as $\phi_k = (\mu_k, \sigma_k^2), k = 1, ..., K$, then the kth conditional Gaussian distribution given the observed histogram distribution $p(y_i), y_i = i = 1, 2, ..., N$ is formulated as:

$$p(x_i \mid y_i, \phi_k) = \frac{1}{\sigma_k \sqrt{2\pi}} e^{-\frac{(x_i - \mu_k)^2}{2\sigma_k^2}}; i = 1, ..., N; k = 1, ..., K$$
 (15)

 g_1 denotes the smallest grayscale value and g_2 denotes the largest grayscale value. Accordingly, the Gaussian mixture model of the histogram is formulated as:

$$p(x_i \mid y_i, \phi) = \sum_{k=1}^{K} p(x_i \mid y_i, \phi_k); i = 1, 2, ..., N$$
 (16)

3.1 The maximum A posteriori method

The maximum A posteriori (MAP) method is a way of computing the maximum likelihood (ML) for the posterior probability of the histogram distribution that is formulated as:

$$p(y_{i} | x_{i}, \phi) = \frac{p(y_{i}) \sum_{k=1}^{K} p(x_{i} | y_{i}, \phi_{k})}{\sum_{i=1}^{N} \left(p(y_{i}) \sum_{k=1}^{K} p(x_{i} | y_{i}, \phi_{k}) \right)}; i = 1, 2, ..., N \quad (17)$$

The denominator part of the above equation is a constant. Thus, to maximize the posterior probability of the histogram distribution is to maximize the numerator part of the above equation, i.e.,

$$p(y_i | x_i, \phi) \propto p(y_i) \sum_{k=1}^{K} p(x_i | y_i, \phi_k); i = 1, 2, ..., N$$
 (18)

The MAP likelihood function is thus formulated as:

$$L(\phi) = \prod_{i=1}^{N} \left(p(y_i) \sum_{k=1}^{K} p(x_i \mid y_i, \phi_k) \right)$$
 (19)

The logarithmic function is used to avoid the above equation approaching 0 infinitely. Accordingly, the logarithmic MAP likelihood function is formulated as:

$$J = \log(L(\phi)) = \sum_{i=1}^{N} p(y_i) \log\left(\sum_{k=1}^{K} p(x_i \mid y_i, \phi_k)\right)$$
(20)

The expectation maximization (EM) method is a systematic method of estimating parameters from incomplete data [8] and it provides a way of determining the ML estimate

of the parameters $\phi_k = (\mu_k, \sigma_k^2), k = 1,..., K$ by updating them iteratively with the following equations [118].

$$\mu_{k} = \sum_{i=1}^{N} \frac{i \times p(y_{i}) \times p(x_{i} \mid y_{i}, \phi_{k})}{p(x_{i} \mid y_{i}, \phi)}$$

$$\sum_{i=1}^{N} \frac{p(y_{i}) \times p(x_{i} \mid y_{i}, \phi_{k})}{p(x_{i} \mid y_{i}, \phi)}$$
(21)

$$\sigma_{k}^{2} = \sum_{i=1}^{N} \frac{\left(i - \mu_{k}\right)^{2} \times \frac{p(y_{i}) \times p(x_{i} \mid y_{i}, \phi_{k})}{p(x_{i} \mid y_{i}, \phi)}}{\sum_{i=1}^{N} \frac{p(y_{i}) \times p(x_{i} \mid y_{i}, \phi_{k})}{p(x_{i} \mid y_{i}, \phi)}}$$
(22)

The EM method exits the iteration until the logarithmic MAP likelihood function converges. After $\phi_k = (\mu_k, \sigma_k^2), k = 1,..., K$ is determined, the thresholds are computed by Eq. (7).

3.2 The least squared error method

The least squared error method computes the minimum of the root squared errors between the histogram distribution $p(y_i)$ and the Gaussian distribution mixture model $p(x_i | y_i, \phi)$ that is formulated by the following equation.

$$J = \sqrt{\sum_{i=1}^{N} (p(y_i) - p(x_i \mid y_i, \phi))^2}$$
 (23)

In the same way, the EM method is used to determine the ML estimate of the parameters $\phi_k = (\mu_k, \sigma_k^2), k = 1,..., K$ by updating them in an iterative way by Eq. (21) and Eq. (22). Then, the iteration is terminated by Eq. (5) or Eq. (6) and the thresholds are computed by Eq. (7).

3.3 The cross-correlation method

If we treat the histogram and the Gaussian mixture model as two continuous signals, h(t) and g(t) respectively, their cross-correlation function [119-120] is formulated as:

$$R_{hg}(\tau) = \int_{-\infty}^{+\infty} h(t) g(t+\tau) dt \tag{24}$$

For the discrete formulations, the histogram is represented as $p(y_i)$ and Gaussian mixture model is represented as $p(x_i | y_i, \phi)$. Thus, the cross-correlation function can be formulated as:

$$J = R_{hg}(0) = \sum_{i=1}^{N} p(y_i) p(x_i | y_i, \phi)$$
 (25)

According to the cross-correlation theory, $R_{hg}(0)$ reaches the maximum value when the histogram and the Gaussian mixture model are most similar. Therefore, Eq. (25) could also be used as the cost function by the EM method to exit the iteration defined by Eq. (5) and Eq. (7) is used to compute the thresholds. The iteration processes of the above three methods are the same, the iteration times are usually different and the accuracies vary insignificantly. The synthesized image shown in Fig. 1 (a) is used to demonstrate the iteration process of the EM-MAP method and the iteration results at different times are

shown in Fig. 2 (a), (b) (c) and (d) respectively. Where "OH-D" represents the histogram distribution of the synthesized image and "GMM-D" represents the Gaussian mixture model distribution formulated by Eq. (16). As can be seen, the shape of the Gaussian mixture model distribution and the shape of the histogram distribution differ greatly in the first iteration while they match quite well in the last iteration.

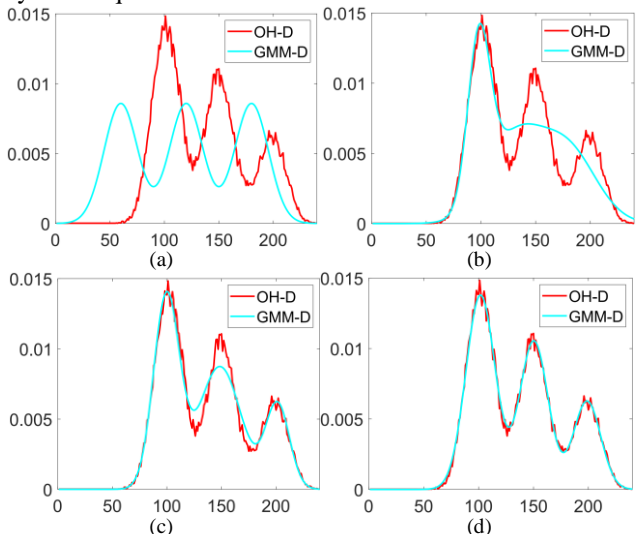


Fig. 2. Demonstration of the iteration process of EM. (a) The results of the 1th iteration; (b) The results of the 20th iteration; (c) The results of the 60th iteration; (d) The results of the 96th iteration.

4. The Entropy-based Method

4.1 The max-entropy-based method

Shannon information entropy is able to quantify the information and represent its uncertainty. In other words, the entropy of the information is proportional to its uncertainty. The Shannon information entropy of the histogram distribution can be formulated as follows.

$$H(y_i) = -\sum_{i=1}^{N} p(y_i) \log(p(y_i))$$
 (26)

The max Shannon entropy methods have been proved to be similar to the maximum-likelihood and Bayesian methods [11]. In histogram-based threshold selection, the max entropy method globally finds the thresholds that make the Shannon information entropy of all the independent pixel classes in the histogram distribution maximum, which can be formulated as:

$$J = -\sum_{i=1}^{T_{1}} p_{1}(y_{i}) \log(p_{1}(y_{i}))$$

$$-\sum_{k=2}^{K-1} \sum_{i=T_{k-1}+1}^{T_{k}} p_{k}(y_{i}) \log(p_{k}(y_{i})) - \sum_{i=T_{K-1}+1}^{N} p_{K}(y_{i}) \log(p_{K}(y_{i}))$$
(27)

The probability distributions $p_k(y_i)$; k = 1, 2, ..., K of the independent pixel classes are computed as follows.

$$p_{k}(y_{i}) = \begin{cases} \frac{p(y_{i})}{\sum_{i=1}^{T_{i}} p(y_{i})}; k = 1; 1 \leq i \leq T_{1} \\ \frac{\sum_{i=1}^{T_{k}} p(y_{i})}{\sum_{i=T_{k-1}+1}^{T_{k}} p(y_{i})}; k = 2, ..., K-1; T_{k-1}+1 \leq i \leq T_{k} \end{cases} (28)$$

$$\frac{i \times p(y_{i})}{\sum_{i=T_{k-1}+1}^{N} p(y_{i})}; k = K; T_{K-1}+1 \leq i \leq N$$

The thresholds $\{T_1, T_2, ..., T_{K-1}\}$ that makes Eq. (27) maximum could be found by a global search. For the image segmentation methods based on other types of entropies [79-100], only the equation (26) of computing the Shannon entropy needs to be replaced by the equation of computing another type of entropy.

4.2 The fuzzy-entropy-based method

Like the max entropy method, the fuzzy entropy method [67-70] also globally finds the thresholds that make the information entropy of all the independent pixel classes in the histogram distribution maximum. Unlike the max entropy method, the fuzzy entropy method adds a fuzzy membership function to its cost function that could be formulated as:

$$J = -\sum_{i=1}^{T_{1}} m_{1} p_{1}(y_{i}) \log(p_{1}(y_{i}))$$

$$-\sum_{k=2}^{K-1} \sum_{i=T_{k-1}+1}^{T_{k}} m_{k} p_{k}(y_{i}) \log(p_{k}(y_{i})) - \sum_{i=T_{K-1}+1}^{N} m_{K} p_{K}(y_{i}) \log(p_{K}(y_{i}))$$
(29)

 m_k denotes the fuzzy membership function and it is computed as follows.

$$m_{k} = \left\{ \left(1 + \frac{\left|i - \sum_{i=1}^{T_{i}} i \times p(y_{i})\right|}{N}\right)^{-1}, k = 1; i = 1, ..., T_{1}$$

$$\left(1 + \frac{\left|i - \sum_{i=T_{k-1}+1}^{T_{k}} i \times p(y_{i})\right|}{N}\right)^{-1}; k = 2, ..., K - 1; i = T_{k-1} + 1, ..., T_{k}$$

$$\left(1 + \frac{\left|i - \sum_{i=T_{k-1}+1}^{N} i \times p(y_{i})\right|}{N}\right)^{-1}; k = K; i = T_{k-1} + 1, ..., N$$

$$i = T_{k-1} + 1, ..., N$$

$$i = T_{k-1} + 1, ..., N$$

The thresholds $\{T_1, T_2, ..., T_{K-1}\}$ that makes Eq. (29) maximum could be found by a global search.

4.3 The cross-entropy-based method

Cross entropy is able to measure the difference between two probability distributions, which makes it important in information theory [13]. The cross entropy distance between a posteriori probability distribution $q(y_i)$ and its priori distribution $p(y_i)$ can be formulated as follows.

$$H_{CE}(q, p) = \sum_{i=1}^{N} q(y_i) \log \left(\frac{q(y_i)}{p(y_i)}\right), i = 1, ..., N$$
 (31)

The metric cross entropy distance can be formulated as follows.

$$H_{m}(q, p) = H_{CE}(q, p) + H_{CE}(p, q) = \sum_{i=1}^{N} q(y_{i}) \log \left(\frac{q(y_{i})}{p(y_{i})}\right) + \sum_{i=1}^{N} p(y_{i}) \log \left(\frac{p(y_{i})}{q(y_{i})}\right)$$
(32)

Based on the cross entropy distance, the cost function can be formulated as follows [78].

$$J = \sum_{i=1}^{T_1} p(y_i) \mu_1 \log\left(\frac{\mu_1}{i}\right) + \sum_{k=2}^{K-1} \sum_{i=T_{k-1}+1}^{T_k} p(y_i) \mu_k \log\left(\frac{\mu_k}{i}\right) + \sum_{i=T_{k-1}+1}^{N} p(y_i) \mu_K \log\left(\frac{\mu_K}{i}\right)$$
(33)

Based on the metric cross entropy distance, the cost function can be formulated as follows [78].

$$J = \sum_{i=1}^{T_1} p(y_i) \left(\mu_1 \log \left(\frac{\mu_1}{i} \right) + i \log \left(\frac{i}{\mu_1} \right) \right)$$

$$+ \sum_{k=2}^{K-1} \sum_{i=T_{k-1}+1}^{T_k} p(y_i) \left(\mu_k \log \left(\frac{\mu_k}{i} \right) + i \log \left(\frac{i}{\mu_k} \right) \right)$$

$$+ \sum_{i=T_{k-1}+1}^{N} p(y_i) \left(\mu_K \log \left(\frac{\mu_K}{i} \right) + i \log \left(\frac{i}{\mu_K} \right) \right)$$
(34)

The thresholds $\{T_1, T_2, ..., T_{K-1}\}$ that makes Eq. (33) or (34) maximum could be found by a global search.

5. The Feature-points-based Method

It is observed that the rate of change at the border of two adjacent pixel classes in a histogram distribution will reach the global maximum or a local maximum. In addition, the rate of change at the center of a pixel-class will also reach the global maximum or a local maximum. On the other hand, the points that yield the global or local maximum rate of change can be treated as the histogram feature points. Thus, the grayscale positions with global or local maximum rates of change are used by the histogram-feature-points-based methods as candidates for computing the clustering means and partitioning thresholds. To avoid too many histogram feature points are detected by the histogram-feature-points-based methods, a histogram is usually smoothed beforehand. Therefore, the histogram needs to be filtered before the histogram-featurepoints-based methods are used to calculate the clustering means and partitioning thresholds.

5.1 Discrete-Fourier-transform-based filtering

The discrete Fourier transform based filter was proved to be the most effective low-pass filter for histogram smoothing [101-102]. In this study, the histogram distribution $p(y_i)$, i = 1, 2, ..., N is rewritten as p(x), x = 1, 2, ..., N. Accordingly, the discrete Fourier transformation X(k) [121-122] of the histogram distribution p(x) can be formulated as follows.

$$X(k) = \sum_{x=1}^{N} p(x)e^{\frac{-j2\pi(k-1)(x-1)}{N}}; k = 1, 2, ..., N$$
 (35)

The inverse discrete Fourier transform is formulated as follows.

$$p(x) = \frac{1}{N} \sum_{k=1}^{N} X(k) e^{\frac{j2\pi(k-1)(x-1)}{N}}; x = 1, 2, ..., N$$
 (36)

Suppose the band width of the discrete Fourier transform filter is W, then the filtered and undistorted histogram p'(x) could be formulated as follows.

$$p'(x) = \frac{1}{N} \sum_{k=1}^{W} X(k) e^{\frac{j2\pi(k-1)(x-1)}{N}} + \frac{1}{N} \sum_{k=N-W+1}^{N} X(k) e^{\frac{j2\pi(k-1)(x-1)}{N}}; x = 1, 2, ..., N$$
(37)

5.2 The histogram-peak-and-valley-based method

When the histogram distribution could be denoted as a Gaussian distribution mixture model, the histogram peak feature points correspond to the mean values of the Gaussian distributed pixel classes and the histogram valley feature points correspond to the thresholds to partition the adjacent Gaussian distributed pixel classes. Suppose the detected histogram peak feature points are denoted as P_k ; k = 1, 2, ..., K, the mean of the kth pixel class in the histogram distribution is computed as:

$$\mu_k = \{ y_i \mid p(y_i) = P_k, i = 1, 2, ..., N \}$$
 (38)

Suppose the detected histogram valley feature points are denoted as V_k ; k = 1, 2, ..., K - 1, the thresholds are computed as:

$$T_k = \{ y_i \mid p(y_i) = V_k, i = 1, 2, ..., N \}$$
 (39)

Besides the equation formulated above, the thresholds could also be computed by Eq. (7).

The synthesized image shown in Fig. 1 (a) is used to demonstrate the histogram peak and valley (HPV) based method in Fig. 3 (a). Where "OH-D" denotes the original histogram distribution of the synthesized image, "FH-D" denotes the filtered histogram distribution formulated by Eq. (36) and "H-axis" denotes the horizontal axis. The grayscale values that correspond to the detected valleys are marked by the red circles and they are the candidate thresholds. In this demo, there are two thresholds, Threshold1 and Threshold2. The grayscales that are corresponding to the detected peaks are marked by the blue crosses and they represent the means, Mean1, Mean2 and Mean3 of the three pixel-classes.

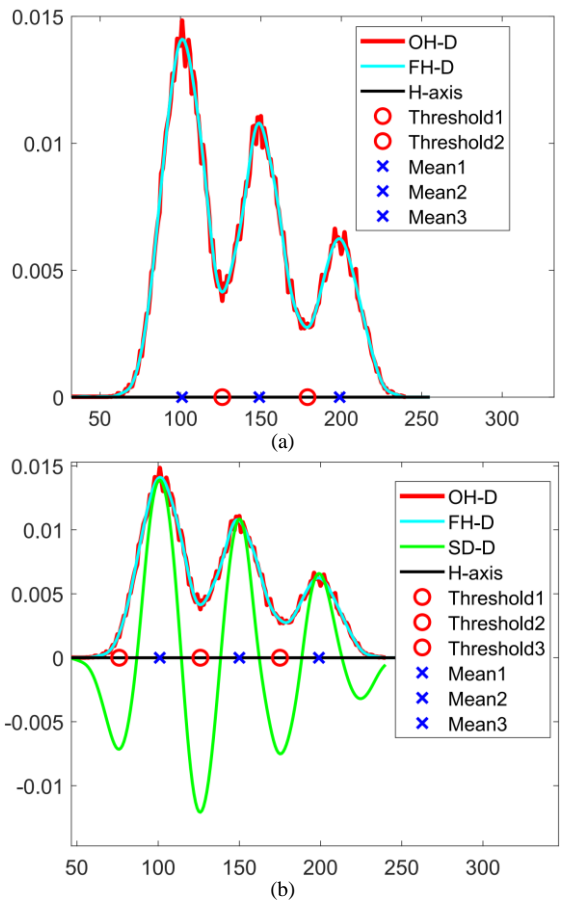


Fig. 3. Demonstration of the rate of change methods. (a) Demonstration of the HPV method; (b) Demonstration of the SDD method.

5.3 The slope-difference-distribution-based method

When the histogram distribution could not be denoted as a Gaussian distribution mixture model, the histogram peak feature points or valley feature points may not exist. In these situations, the HPV method will not work. To solve this problem, the slope difference distribution (SDD) method was proposed [101] and it can be summarized as follows.

For the *i*th point of the smoothed histogram distribution p'(x); x = 1, 2, ..., N, we compute two slopes for it by fitting two lines on its left side and on its right side respectively. The line equation is defined as follows.

$$l = ax + b \tag{40}$$

The coefficients $[a,b]^T$ of the line model are computed by the least squared fitting as follows.

$$\left[a, b \right]^{\mathsf{T}} = \left(B^{\mathsf{T}} B \right)^{-1} B^{\mathsf{T}} Y$$
 (41)

For the left fitted line, B and Y are formulated as follows.

$$B = \begin{bmatrix} i - Q + 1 & 1 \\ i - Q + 2 & 1 \\ \vdots & \vdots \\ i & 1 \end{bmatrix}$$

$$(42)$$

$$Y = \left[p'(i-Q+1), p'(i-Q+2), ..., p'(i) \right]^{T}$$
 (43)

Where Q denotes the number of the selected points on the left of the *i*th point. For the right fitted line, B and Y are formulated by the following equation.

$$B = \begin{bmatrix} i & 1\\ i+1 & 1\\ \vdots & \vdots\\ i+Q-1 & 1 \end{bmatrix}$$

$$(44)$$

$$Y = \left[p'(i), p'(i+1), ..., p'(i+Q-1) \right]^{T}$$
 (45)

Where Q denotes the number of the selected points on the right of the ith point. The slope difference at the ith point is then calculated by the following equation.

$$S_d(i) = a_{right}(i) - a_{left}(i); i = 1 + Q, ..., N - Q$$
 (46)

Where $a_{right}(i)$ denotes the slope of the line fitted by the points selected on the right of the *i*th point and $a_{left}(i)$ denotes the slope of the line fitted by the points selected on the left side of the *i*th point. The derivative of the slope difference distribution $S_d(x)$ is computed and set to zero as follows.

$$\frac{dS_d(x)}{dx} = 0\tag{47}$$

Both the peak feature points P_k ; k = 1, 2, ..., K and the valley feature points V_k ; k = 1, 2, ..., K-1 of $S_d(x)$ can be calculated by solving the above equation. The means $\{\mu_1, \mu_2, ..., \mu_K\}$ are then calculated by Eq. (38) and the thresholds are then calculated by Eq. (39) or Eq. (7).

The synthesized image shown in Fig. 1 (a) is used to demonstrate the SDD method in Fig. 3 (b). Where "OH-D" denotes the original distribution of the histogram for the synthesized image, "FH-D" denotes the filtered distribution of the histogram formulated by Eq. (36) and "SD-D" denotes the distribution of the slope difference computed by Eq. (46). It is seen that the thresholds and the means calculated by the SDD method and by the HPV method are very similar for the histogram with the Gaussian mixture model distribution. However, the HPV method may not compute the thresholds or means as accurate as the SDD method when the histogram shapes become irregular, which will be demonstrated in the following sections.

6. Experimental Results

6.1 Quantitative evaluation of the histogram-based methods in segmenting the synthesized images

In this section, the performances of the image segmentation methods based on histograms are evaluated quantitatively by segmenting the synthesized images since the histogram shapes and the parameters of the synthesized images could be controlled precisely. Three quantitative measures are computed to compare the accuracies of these methods. The first quantitative measure is called dice similarity coefficient (DSC) that is formulated as follows.

$$DSC = \frac{2 \times S \cap G}{S + G} \tag{48}$$

where S denotes the computed area of the segmented object and G denotes the ground truth area.

The second quantitative measure is called average perpendicular distance (APD) that is formulated as follows.

$$APD = \frac{1}{N_S} \sum_{i=1}^{N_S} \underset{j=1,2,...,N_G}{\arg \min} \left| P_i^S - P_j^G \right|$$
 (49)

where P_i^s represents the *i*th point of the segmented object's boundary and P_j^G denotes the *j*th point on the groundtruth boundary. N_s represents the total number of the points on the boundary of the segmented object and N_G represents the total number of the points on the ground truth boundary.

The third quantitative measure is called average mean difference (AMD) that is formulated as follows.

$$AMD = \frac{1}{N_{I} \times N_{II}} \sum_{i=1}^{N_{I}} \sum_{i=1}^{N_{\mu}} |\mu_{S}(i,j) - \mu_{G}(i,j)|$$
 (50)

 $\mu_s(i,j)$ represents the *j*th computed mean value for the *i*th image. $\mu_G(i,j)$ represents the *j*th ground-truth mean value in the *i*th image. N_I represents the total number of the images used to compute the pixel means and N_μ represents the total number of the pixel means in each image.

The synthesized image is demonstrated in Fig. 1 (a). The mean value of the first pixel class, i.e., the background is 100. The mean value of the second pixel class, i.e., the two smaller rectangles is 150. The mean value of the third pixel class, i.e., the largest rectangle is 200. Then the Gaussian noises are added by multiplying the standard normal distribution with the amplitude varying from 11 to 90. The parameters of the synthesized image sets are denoted as {100,150,200; [11,90]} in this tutorial. The quantitative accuracies of these image segmentation methods based on histograms are compared in Table 1. In addition to comparing the methods of the same class, we also compare them with three generalized image segmentation methods based on deep learning. The three compared methods based on deep learning are cellpose [123]. the multiple instance learning (MIL) framework [124] and the segment anything model (SAM) [125]. It is seen that the fuzzy-Cmeans method achieved the highest DSC score and the lowest APD error while SDD achieved the lowest AMD error. The Kmeans method, the EM methods, the max entropy method and the fuzzy entropy method achieved poor segmentation performances. To analyze the possible reasons that caused the poor performances of these methods, we plot the representative histograms of the synthesized images in Fig. 4 (a) and we plot their DSC scores in Fig. 4 (b). It is seen that the max entropy method performed badly for the first 15 images and the fuzzy entropy method performed badly for the first 16 images. The Kmeans method performed badly for the first 22 images and the EM methods performed badly for the first 32 images.

Table 1. Comparison of the segmentation accuracies for different methods with the synthesized image sets {100,150,200; [11,90]}. (The bold values represent the best performances)

represent the best performances)				
Method	DSC	APD	AMD	
DL-cellpose	0.9695	1.5236	NA	
DL-MIL	0.9618	1.8543	NA	
DL-SAM	0.9816	0.9654	NA	
K-means	0.8622	6.4877	41.6279	
Otsu	0.9769	1.0299	3.8624	
Fuzzy-Cmeans	0.9770	1.0313	3.9187	
EM-MAP	0.8065	9.2061	42.1319	
EM-LSE	0.8065	9.2004	45.4919	
EM-CC	0.8064	9.1939	44.5058	
Max Entropy	0.8560	15.4130	132.3552	
Fuzzy Entropy	0.8496	16.1229	132.2897	
Cross Entropy 1	0.9766	1.0268	6.6674	
Cross Entropy 2	0.9766	1.0268	6.7041	
HPV	0.9718	1.3637	3.4500	
SDD	0.9765	1.0862	2.1875	

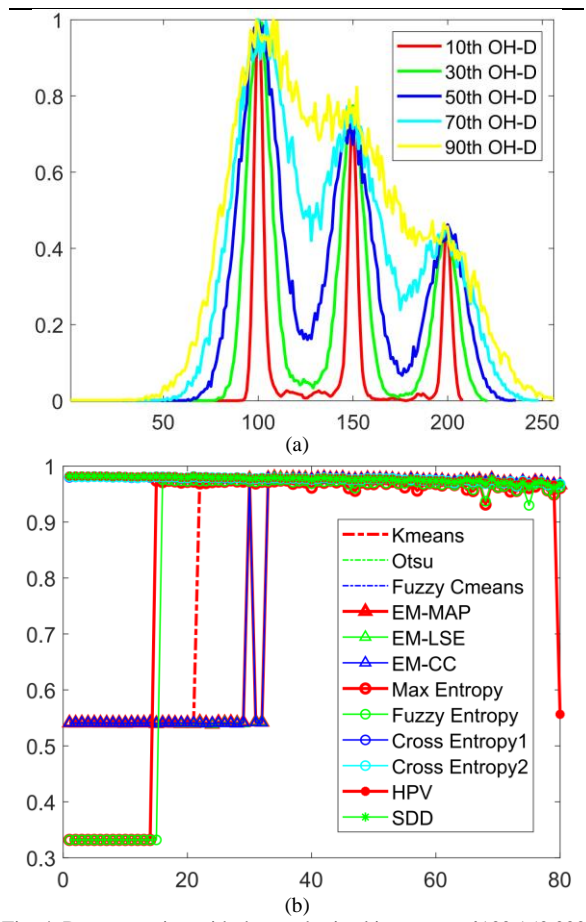


Fig. 4. Demonstration with the synthesized image sets {100,150,200; [11,90]}. (a) The histograms of the 10th synthesized image, the 30th synthesized image, the 50th synthesized image, the 70th synthesized image and the 90th synthesized image; (b) The computed DSC scores of the histogrambased image segmentation methods.

Table 2. Comparison of the segmentation accuracies for different methods with the synthesized image sets {50,120,200; [11,90]}. (The bold values

represent the best performances)				
Method	DSC	APD	AMD	
DL-cellpose	0.9724	1.3760	NA	
DL-MIL	0.9644	1.8231	NA	
DL-SAM	0.9841	0.7072	NA	
K-means	0.9799	0.7970	3.9048	
Otsu	0.9799	0.7964	3.9261	
Fuzzy-Cmeans	0.9799	0.7973	2.9940	
EM-MAP	0.9798	0.8013	4.1658	
EM-LSE	0.9798	0.8013	4.1678	
EM-CC	0.9798	0.8020	4.3153	
Max Entropy	0.9756	1.1114	45.4902	
Fuzzy Entropy	0.9771	0.8360	29.0177	
Cross Entropy 1	0.9788	0.8002	5.2548	
Cross Entropy 2	0.9791	0.7940	5.1844	
HPV	0.9802	0.7995	2.1000	
SDD	0.9801	0.8039	2.2750	

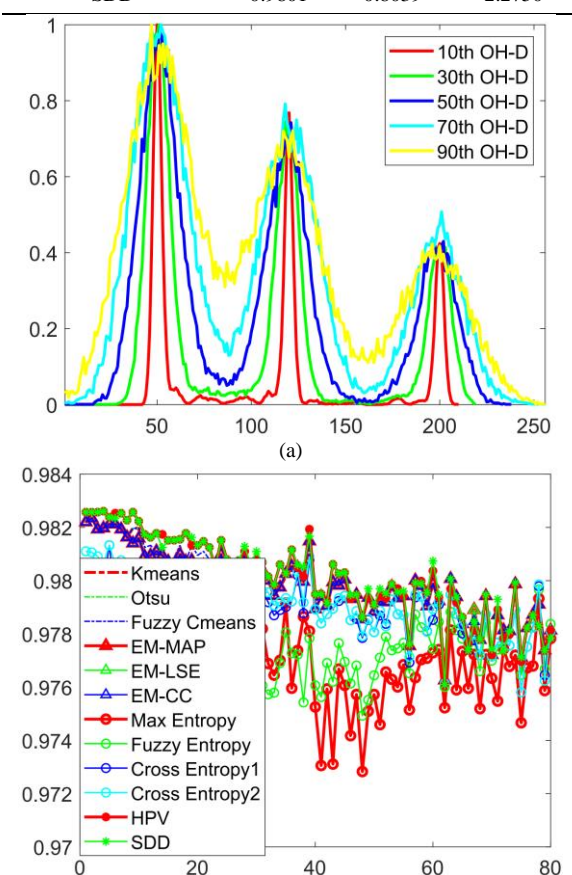


Fig. 5. Demonstration with the synthesized image sets {50,120,200; [11,90]}. (a) The histograms of the 10th synthesized image, the 30th synthesized image, the 50th synthesized image and the 90th synthesized image; (b) The computed DSC scores of the histogram-based image segmentation methods.

(b)

For comparison, we change the parameters of the synthesized image sets from {100,150,200; [11,90]} to {50,120,200; [11,90]}, i.e., we enlarge the distances between

the adjacent pixel classes. The quantitative accuracies of these methods are shown in Table 2. It is seen that all these histogram-based image segmentation methods performed better and none of them performed badly anymore. To see the differences more clearly, we plot the representative histograms of the corresponding synthesized images in Fig. 5 (a) and we plot the DSC scores in Fig. 5 (b). It is seen that the histograms look similar except that the spacing between adjacent pixel classes becomes larger. The performances of most methods declined gradually with reference to the augments of the noise amplitude. In summary, the performances of these methods are affected by the shapes of the histograms as demonstrated in Figs. 4-5.

We merge the background and the two smaller rectangles as the first pixel class and select their mean as 50. The pixels in the largest rectangle belong to the second pixel class and we select their mean as 200. The parameters of the synthesized image sets become {50,200; [11,90]}. The quantitative accuracies of these methods are shown in Table 3. It is seen that all these methods except the max entropy method performed well. If we change the parameter of the synthesized image sets to {150,200; [11,90]}, the K-means method, the EM methods, the max entropy method and the fuzzy entropy method will achieve poor segmentation performances.

Table 3. Comparison of the segmentation accuracies for different methods with the synthesized image sets {50,200; [11,90]}. (The bold values represent

the best performances)				
Method	DSC	APD	AMD	
DL-cellpose	0.9736	1.3173	NA	
DL-MIL	0.9654	1.7713	NA	
DL-SAM	0.9908	0.1215	NA	
K-means	0.9867	0.1668	2.1903	
Otsu	0.9867	0.1665	2.1903	
Fuzzy-Cmeans	0.9870	0.1484	1.6915	
EM-MAP	0.9868	0.1598	2.3886	
EM-LSE	0.9868	0.1597	2.3894	
EM-CC	0.9868	0.1598	2.3892	
Max Entropy	0.8733	12.1279	8.5604	
Fuzzy Entropy	0.9392	4.7990	3.7257	
Cross Entropy 1	0.9825	0.3649	2.6484	
Cross Entropy 2	0.9842	0.2796	2.5467	
HPV	0.9815	1.0076	0.5250	
SDD	0.9871	0.1470	0.6500	

From the quantitative comparisons shown in Tables 1-3, the deep-learning-based SAM method achieved the best accuracy while the other two deep learning methods achieved the low-ranking accuracies. The overall accuracy of the image segmentation methods based on histograms is higher than that of the image segmentation methods based on deep learning [123-125] in segmenting the synthesized images with uniform backgrounds. However, the performances of some histogram-based methods may rely heavily on the shapes of the histograms. The mean computation time of each method is evaluated by segmenting 80 synthesized images of 3 means and 2 means respectively in MATLAB. The means of the computation time for these methods are shown in Table 4. The EM cross

correlation method achieved the best performance and the fuzzy entropy method achieved the worst performance. Since the three compared deep-learning-based image segmentation methods are not implmented in MATLAB, their computation time are not available.

Table 4. Comparison of the means of the computation time for different methods in segmenting the synthesized images with three pixel-classes and two pixel-classes respectively. (The bold values represent the best

•	performances)	
Method	3 means 2 means	
	(millisecond)	(millisecond)
K-means	0.52952	0.4145
Otsu	19.72625	0.5436
Fuzzy-Cmeans	1.09268	1.0274
EM-MAP	1.31419	0.4263
EM-LSE	1.00461	0.3731
EM-CC	0.46399	0.3535
Max Entropy	618.60540	1.9638
Fuzzy Entropy	1057.87737	1.9015
Cross Entropy 1	779.31426	2.6434
Cross Entropy 2	627.54222	1.6155
HPV	1.78593	0.6650
SDD	20.25115	5.6821

6.2 Quantitative evaluation of the histogram-based methods in segmenting the real images

Table 5. Comparison of the segmentation accuracies for different methods with the MICCAI MRI dataset. (The bold values represent the best

performances)				
Method	DSC	APD		
DL-cellpose	0.8883	2.6939		
DL-MIL	0.8853	2.7785		
DL-SAM	0.8987	2.7668		
K-means	0.9068	2.1845		
Otsu	0.9073	2.1773		
Fuzzy-Cmeans	0.9086	2.1473		
EM-MAP	0.9046	2.3777		
EM-LSE	0.9051	2.3523		
EM-CC	0.9070	2.2037		
Max Entropy	0.9187	1.9206		
Fuzzy Entropy	0.9041	2.2339		
Cross Entropy 1	0.8929	2.7597		
Cross Entropy 2	0.8681	3.7335		
HPV	0.8978	2.5144		
SDD	0.9255	1.7700		

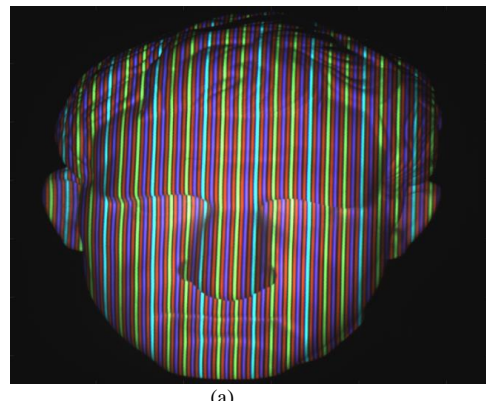
In this section, the performances of the image segmentation methods based on histograms are evaluated quantitatively in segmenting the real images with simple or uniform backgrounds from different applications. The first image dataset is from cardiac left ventricle (LV) segmentation challenge [126] which is available online. 117 nuclear magnetic resonance imaging (MRI) images of the left ventricle at the enddiastolic stage or at the end-systolic stage are selected from the

dataset. The quantitative accuracies of the image segmentation methods based on histograms and the image segmentation methods based on deep learning are compared in Table 5. It is seen that the SDD method achieved the best performance after the rules of the selecting the thresholds were designed according to the characteristics of the MRI images [102]. Most histogram-based image segmentation methods achieved better accuracies compared to the deep-learning methods [123-125].

Table 6. Comparison of the segmentation accuracies for different methods with the NUS hand dataset I. (The bold values represent the best

Method	DSC	APD
DL-cellpose	0.6255	50.5058
DL-MIL	0.9680	0.8109
DL-SAM	0.9885	0.2267
K-means	0.9891	0.4253
Otsu	0.9891	0.4253
Fuzzy-Cmeans	0.9883	0.2879
EM-MAP	0.9880	0.2107
EM-LSE	0.9787	0.3302
EM-CC	0.9787	0.3302
Max Entropy	0.9617	2.3615
Fuzzy Entropy	0.9787	0.3302
Cross Entropy 1	0.9889	0.5908
Cross Entropy 2	0.9889	0.5908
HPV	0.3255	80.0061
SDD	0.9860	0.510

The second image dataset is from the National University of Singapore (NUS) [127] which is available online. It is composed of 240 images of hand gestures in 10 classes. All the hand gesture images are with uniform background and they were captured by a CCD camera. The quantitative accuracies of different methods are compared in Table 6. It is seen that the Kmeans method and the Otsu method achieved the best DSC. The EM-MAP method achieved the best APD. The HPV method achieved the worst accuracy because there are no valleys in the smoothed histograms. The cellpose deep-learning-based image segmentation method achieved the second worst accuracy because it was trained to segment simple shapes. Overall, the histogram-based image segmentation methods are more accurate than the deep-learning-based image segmentation methods [123-125] in this application.



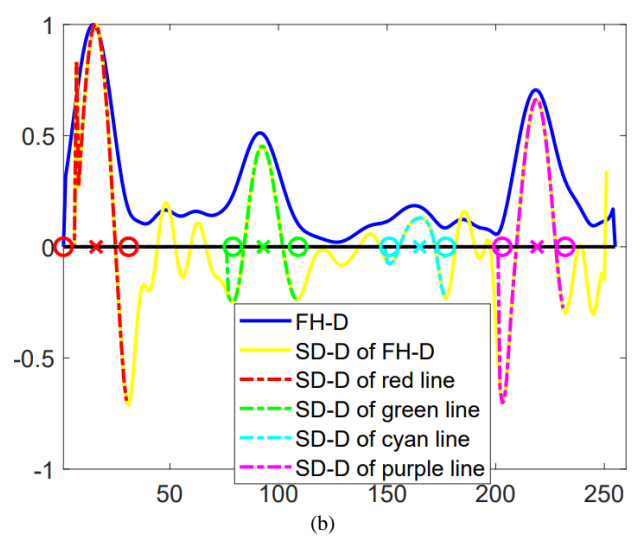


Fig. 6. Demonstration of the SDD method in segmenting a color line image.

(a) A selected color line image; (b) The process of selecting the double SDD thresholds for different color lines.

The third image dataset is from our lab. It consists of 100 color line images. Different from the first two image datasets, multiple thresholds instead of one are required to segment different color lines. The color line image contains the purple,

red, cyan and red lines that need to be segmented and clustered for real-time 3D reconstruction. Since this image dataset is not available online, we demonstrate a typical color line image in Fig. 6 (a). The brightness of the color line image is eliminated by the transformation of the RGB model to the HSV model. Then, the H channel is used to segment different color lines. The histogram of the color line image and its slope difference distribution are shown in Fig. 6 (b). It is seen that the pixel distribution of every type of color line follows the Gaussian distribution well. For the SDD method, the double thresholds are determined by the two valleys on both sides of the SDD peak computed for each type of color line. For other histogrambased methods, the double thresholds are determined by assigning a fixed range on both sides of the computed means. Based on trial and analysis, the fixed range is selected as [-15 15]. The quantitative accuracies of the histogram-based image segmentation methods are compared in Table 7 and we did not compare the deep-learning-based image segmentation methods because they could not generate meaningful segmentation results in this application. It is seen that the SDD method achieved the highest DSC scores. Both the SDD method and the HPV method perform better than other histogram-based methods in this application.

Table 7. Comparison of the segmentation accuracies for different methods with the color line image dataset. (The bold values represent the best performances)

Method	DSC	DSC	DSC	DSC	Average DSC
	red lines	green lines	cyan lines	purple lines	
K-means	0.9754	0.8723	0.9248	0.9401	0.9282
Otsu	0.8360	0.8467	0.9258	0.9392	0.8869
Fuzzy-Cmeans	0.9754	0.8723	0.9248	0.9401	0.9282
EM-MAP	0.9873	0.6980	0.9460	0.9466	0.8945
EM-LSE	0.9873	0.6979	0.9460	0.9466	0.8944
EM-CC	0.9873	0.6981	0.9459	0.9466	0.8945
Max Entropy	0.0032	0.0000	0.5341	0.9187	0.3640
Fuzzy Entropy	0.9720	0.8837	0.8890	0.9401	0.9212
Cross Entropy 1	0.9809	0.8012	0.8839	0.9436	0.9024
Cross Entropy 2	0.9800	0.8012	0.8870	0.9436	0.9030
HPV	0.9880	0.9699	0.9662	0.9678	0.9730
SDD	0.9880	0.9721	0.9576	0.9750	0.9732

The fourth image dataset is from the combined healthy abdominal organ segmentation (CHAOS) 2019 [128] which is available online. There are 20 batches of computed tomography (CT) liver images. One hundred images are selected to compare the image segmentation methods based on histograms and the image segmentation methods based on deep learning [123-125]. As it turned out, only the SDD method and the fuzzy C-means method could achieve meaningful segmentation results for the selected CT images. Two typical CT liver images are demonstrated in Figs. 7 (a)-(b) respectively. The ground truth contour of the liver delineated by the medical experts is represented by the red curve, the contour of the liver segmented by the SDD method is represented by the green curve and the contour of the liver segmented by the fuzzy Cmeans method is represented by the blue curve. Both methods compute two thresholds to segment the liver. The process of the compute the double thresholds by the SDD method is demontrated in Figs. 7 (c)-(d) respectively. It is seen that the distance between the liver pixel class and its adjacent pixel class is very small, which causes most the histogram-based image segmentation methods to treat them as one class. The double thresholds selected by the SDD method are denoted by the purple asterisks. The fuzzy C-means method also caculates two thresholds to segment the liver in the same way. The DSC computed by the SDD method on the selected 100 CT liver image is 0.9822 and the DSC computed by the fuzzy C-means method is 0.9824, which is very close. The APD computed by the SDD method on the selected 100 CT liver image is 1.5515 and the APD computed by the fuzzy C-means method is 1.5127, which is also very close. All the compared deep learning methods failed to yield meaningful results of the livers. We show the results of the DL-SAM method in Fig. 8 for comparison. It is seen that the DL-SAM method could not segment the livers robustly, which has aslo been reported in

recent studies [129].

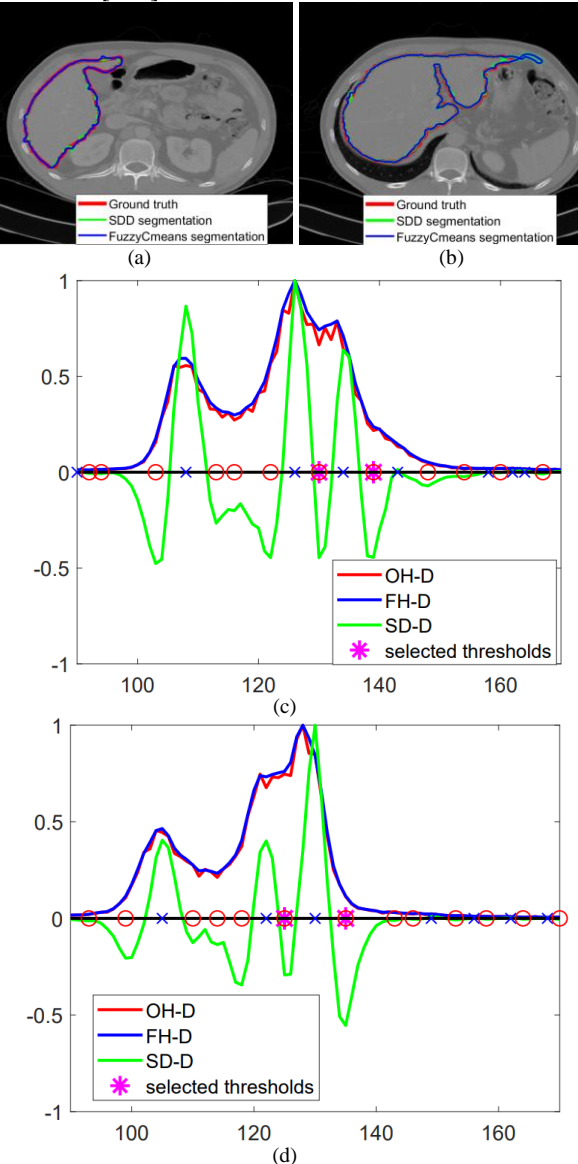


Fig. 7. Demonstration of the SDD method in segmenting the CT liver image.

(a) A selected CT liver image with the ground-truth-contour and the segmented-contours- superimposed onto it; (b) Another selected CT liver image with the ground-truth-contour and the segmented-contours superimposed onto it; (c) The process of selecting the double SDD thresholds;

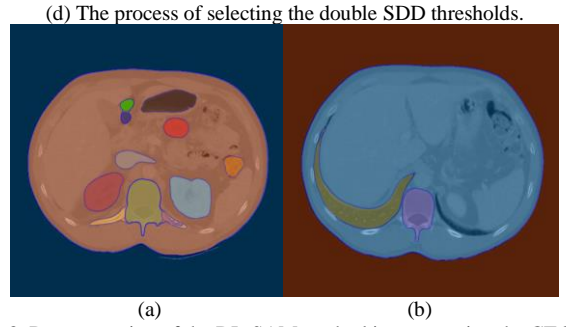


Fig. 8. Demonstration of the DL-SAM method in segmenting the CT liver image. (a) Results of segmenting the first liver image; (b) Results of segmenting the second liver image.

6.3 Discussion

Despite the great advancement of the deep learning methods in recent years, image segmentation is still challenging because of the facts that (1), the grayscales of different images vary greatly, which causes the histogram of the image to vary irregularly and greatly. (2), the target objects may not be isolated from the background, which causes the image segmentation results to be not perfect. (3), the grayscales inside the target objects vary greatly and the background is complex, which causes image segmentation to fail. Based on the experimental results and comparisons in this article, we could draw the following conclusions.

- (1), there is not one single histogram-based image segmentation technique that can always achieve the best performance in all comparisons.
- (2), the performances of the histogram-based image segmentation techniques are affected by the histogram shapes greatly. Among them, fuzzy C-means and SDD could adapt to a variety of histogram shapes while other histogram-based image segmentation techniques could not.
- (3), Without special training, the overall performance of the histogram-based image segmentation techniques is often better than the overall performance of the deep learning methods in the segmenting the images with uniform or simple backgrounds.
- (4), With special training, the deep learning methods could achieve better accuracies in segmenting almost any types of images compared to the histogram-based methods. Combining the histogram-based image segmentation methods with deep learning will be a potential way to address their limitations.

7. Conclusion

This article provided a review of the histories and recent advances of the histogram-based image segmentation techniques. Their working principles were then described in a comparative way. Extensive experiments have been conducted to compare the performances of the histogram-based image segmentation methods and three representative deep learning methods. The advantages and disadvantages of these techniques could be seen clearly with the extensive comparisons. The reason why so many image segmentation techniques have been developed so far is that there is not one single technique that is able to solve the segmentation problem thoroughly.

CRediT authorship contribution statement

Zhenzhou Wang contributed all.

Funding

This research work did not receive any external funding.

Declaration of competing interest

The authors declare that they not have any known competing interests.

Data availability

The data and codes are available upon reasonable request.

References

- [1] Z. Z. Wang, "A tutorial on single-shot 3D surface imaging techniques [Lecture Notes]," in *IEEE Signal Processing Magazine*, vol. 41, no. 1, pp. 71-92, Apr. 2024.
- [2] Z. Z. Wang, "Single-shot 3D reconstruction by fusion of Fourier transform profilometry and line clustering," in *IEEE Journal of Selected Topics in Signal Processing*, vol. 18, no. 3, pp. 325-335, Apr. 2024.
- [3] Z. Z. Wang, "Review of real-time three-dimensional shape measurement techniques," in *Measurement*, vol. 156, pp. 107624, May 2020.
- [4] J.G. Jiang, J. W. Zhang, J. P. Sun, D. H. Wu and S. N. Xu, "User's image perception improved strategy and application of augmented reality systems in smart medical care: A review," in *The International Journal of Medical Robotics and Computer Assisted Surgery*, vol. 19, no. 3, pp. e2497, Jan. 2023.
- [5] A. Balasundaram, S. Routray, A. V. Prabu, P. Krishnan, P. P. Malla and M. Maiti, "Internet of things (IoT)-based smart healthcare system for efficient diagnostics of health parameters of patients in emergency care," in *IEEE Internet of Things Journal*, vol. 10, no. 21, pp. 18563-18570, Nov. 2023.
- [6] E. W. Forgy, "Cluster analysis of multivariate data: efficiency versus interpretability of classifications," in *Biometrics*. vol. 21, no. 3, pp.768– 769, 1965.
- [7] G. B. Coleman and H. C. Andrews, "Image segmentation by clustering," in *Proceedings of the IEEE*, vol. 67, no. 5, pp. 773-785, May. 1979.
- [8] A. P. Dempster, N. M. Laird, and D. B. Rubin, "Maximum likelihood from incomplete data via the EM algorithm," in *Journal of the Royal Statistical Society: Series B (Methodological)*, vol. 39, no. 1, pp. 1–38, 1977.
- [9] N. Ostu, "A threshold selection method from gray-level histograms," in *IEEE Trans SMC*, vol. 9, no. 1, Jan. 1979.
- [10] J. C. Bezdek, R. Ehrlich and W. Full, "FCM: The fuzzy c-means clustering algorithm," in *Computers & geosciences*. vol. 10, no. 2-3, pp. 191-203, 1993.
- [11] E. T. Jaynes, "On the rationale of maximum-entropy methods," in *Proceedings of the IEEE*, vol. 70, no. 9, pp. 939-952, Sep. 1982.
- [12] T. Pun, "A new method for grey-level picture thresholding using the entropy of the histogram," in *Signal processing*, vol. 2, no. 3, pp. 223-237, Jul. 1980.
- [13] J. Shore and R. Johnson, "Properties of cross-entropy minimization," in *IEEE Transactions on Information Theory*, vol. 27, no. 4, pp. 472-482, Jul. 1981.
- [14] A. Rosenfeld and P. De La Torre, "Histogram concavity analysis as an aid in threshold selection," in *IEEE Transactions on Systems, Man, and Cybernetics*, vol. SMC-13, no. 2, pp. 231-235, Mar.-Apr. 1983.
- [15] A. Kumar, A. Kumar, R. Mallipeddi and D. G. Lee, "High-density cluster core-based k-means clustering with an unknown number of clusters," in *Applied Soft Computing*, vol. 155, pp. 111419, Apr. 2024.
- [16] M. I. Faizi and S. M. Adnan, "Improved segmentation model for melanoma lesion detection using normalized cross-correlation-based kmeans clustering," in *IEEE Access*, vol. 12, no. 20, pp. 20753-20766, 2024.
- [17] P. Fränti and S. Sami, "How much can k-means be improved by using better initialization and repeats?." *Pattern Recognition* 93 (2019): 95-112.
- [18] Mousa, W. A. (2024). First Arrival Picking of Exploration Seismic Data Using Pseudo-coloring and Color Image Segmentation. *IEEE Geoscience* and Remote Sensing Letters.
- [19] J. Saha and M. Jayanta , "CNAK: Cluster number assisted K-means." Pattern Recognition 110 (2021): 107625.
- [20] Viprav B. Raju, Masudul H. Imtiaz, Edward Sazonov, "Food Image Segmentation Using Multi-Modal Imaging Sensors with Color and Thermal Data", Sensors, vol.23, no.2, pp.560, 2023.
- [21] Khan, Z., & Yang, J. (2024). Nonparametric K-means clustering-based adaptive unsupervised colour image segmentation. *Pattern Analysis and Applications*, 27(1), 17.
- [22] J. Heidari, N. Daneshpour and A. Zangeneh. "A novel K-means and K-medoids algorithms for clustering non-spherical-shape clusters non-sensitive to outliers." *Pattern Recognition* (2024): 110639.
- [23] M. Rezaei and F. Pasi, "K-sets and k-swaps algorithms for clustering sets." *Pattern Recognition* 139 (2023): 109454.

- [24] J. B. Zang, T. Cai, C. Zong, G. Yang, Z. Zhang and C. Y. Xue, "Tuberculin skin test result detection method based on CSN-II and improved OTSU method," in *Measurement*, vol. 229, pp. 1114409, Apr. 2024.
- [25] X. L. Liu, Z. L. Zhang, Y. F. Hao, H. Zhao and Y. Yang, "Optimized OTSU segmentation algorithm-based temperature feature extraction method for infrared images of electrical equipment," in *Sensors*, vol. 24, no. 4, pp. 1126, Feb. 2024.
- [26] M. J. Garde, P. S. Patil, "Multi-level thresholding segmentation based on levy horse optimized machine learning approach", *Multimedia Tools and Applications*, 2024.
- [27] Gharehchopogh, F.S. and Ibrikci, T., 2024. An improved African vultures optimization algorithm using different fitness functions for multi-level thresholding image segmentation. *Multimedia Tools and Applications*, 83(6), pp.16929-16975.
- [28] Lei, B., Zhang, H., Li, T., Liu, S., Zhang, M., & Xu, X. (2024). A new image segmentation method by minimizing normalized total variation. *Digital Signal Processing*, 146, 104361.
- [29] Akan, T., Oliva, D., Feizi-Derakhshi, A. R., Feizi-Derakhshi, A. R., Pérez-Cisneros, M., & Bhuiyan, M. A. N. (2024). Battle royale optimizer for multilevel image thresholding. *The Journal of Supercomputing*, 80(4), 5298-5340.
- [30] Abualigah, L., Al-Okbi, N. K., Awwad, E. M., Sharaf, M., & Daoud, M. S. (2024). Boosted Aquila Arithmetic Optimization Algorithm for multi-level thresholding image segmentation. *Evolving Systems*, 1-28.
- [31] Mostafa, R. R., Houssein, E. H., Hussien, A. G., Singh, B., & Emam, M. M. (2024). An enhanced chameleon swarm algorithm for global optimization and multi-level thresholding medical image segmentation. *Neural Computing and Applications*, 36(15), 8775-8823.
- [32] Li, H., Qiao, T., & Ding, X. (2024). Effect of grayscale threshold on X-ray computed tomography reconstruction of gas diffusion layers in polymer electrolyte membrane fuel cells. *Heliyon*, 10(7).
- [33] Chauhan, D., & Yadav, A. (2023). A crossover-based optimization algorithm for multilevel image segmentation. Soft Computing, 1-33.
- [34] Y. M. Tang, F. J. Ren and W. Pedrycz, "Fuzzy C-means clustering through SSIM and patch for image segmentation," in *Applied Soft Computing*, vol. 87, pp. 105928, Feb. 2020.
- [35] H. Y. Yu, L. R. Jiang, J. L. Fan, S. Xie and R. Lan, "A feature-weighted suppressed possibilistic fuzzy c-means clustering algorithm and its application on color image segmentation," in *Expert Systems with Applications*, vol. 241, pp. 122270, May. 2024.
- [36] H. Y. Yu, S. Xie, J. L. Fan, R. Lan and B. Lei, "Mahalanobis-kernel distance-based suppressed possibilistic C-means clustering algorithm for imbalanced image segmentation," in *IEEE Transactions on Fuzzy Systems*, vol. 32, no. 8, pp. 4595-4609, Aug. 2024.
- [37] H. C. Sun, L. Liu and F. Z. Li, "A lie group semi-supervised FCM clustering method for image segmentation," in *Pattern Recognition*, vol. 155, pp. 110681, Nov. 2024.
- [38] T. Lei, X. Jia, Y. Zhang, S. Liu, H. Meng and A. K. Nandi, "Superpixel-Based Fast Fuzzy C-Means Clustering for Color Image Segmentation," in *IEEE Transactions on Fuzzy Systems*, vol. 27, no. 9, pp. 1753-1766, Sept. 2019, doi: 10.1109/TFUZZ.2018.2889018.
- [39] R.X. Zhang, Y. Duan, F. P. Nie, R. Wang, X.L. Li, "Unsupervised Deep Embedding for Fuzzy Clustering", *IEEE Transactions on Fuzzy Systems*, vol.32, no.12, pp.6744-6753, 2024.
- [40] J. J. Jiao, X. P. Wang, T. Y. Wei, J. P. Zhang, "An Adaptive Fuzzy C-Means Noise Image Segmentation Algorithm Combining Local and Regional Information", *IEEE Transactions on Fuzzy Systems*, vol.31, no.8, pp.2645-2657, 2023.
- [41] C. Q. Huang, H. Lei, Y. Chen, J. H. Cai, X. S. Qin, J. L. Peng, L. H. Zhou and L. Zheng, "Interval Type-2 enhanced possibilistic fuzzy C-means noisy image segmentation algorithm amalgamating weighted local information", *Engineering Applications of Artificial Intelligence*, vol.137, pp.109135, 2024.
- [42] B. Yu, Z. J. Zheng, M. J. Cai, W. Pedrycz, W.P. Ding, "FRCM: A fuzzy rough c-means clustering method", *Fuzzy Sets and Systems*, pp.108860, 2024.
- [43] A. Farooq and K. H. Memon, "Kernel possibilistic fuzzy c-means clustering algorithm based on morphological reconstruction and membership filtering", Fuzzy Sets and Systems, vol. 477, pp. 108792, 2024.
- [44] E. Janusonis, G. Kazakeviciute-Januskeviciene, R. Bausys, "Selection of Optimal Segmentation Algorithm for Satellite Images by Intuitionistic Fuzzy PROMETHEE Method", *Applied Sciences*, vol.14, no.2, pp.644, 2024.

- [45] L. Guo, P. F. Shi, L. Chen, C. Chen, W. P. Ding, "Pixel and region level information fusion in membership regularized fuzzy clustering for image segmentation", *Information Fusion*, vol.92, pp.479, 2023.
- [46] H. Y. Yu, X. Y. Xu, H. L. Li, Y. T. Wu, B. Lei, "Semi-Supervised Possibilistic c-Means Clustering Algorithm Based on Feature Weights for Imbalanced Data", *Knowledge-Based Systems*, pp.111388, 2024.
- [47] C. M. Wu, J. T. Zhao, "Robust joint learning of superpixel generation and superpixel-based image segmentation using fuzzy C-multiple-means clustering", Signal, Image and Video Processing, 2023.
- [48] A. Das, A. Namtirtha, A. Dutta, "Membership Adjusted Superpixel Based Fuzzy C-Means for White Blood Cell Segmentation", *Pattern Recognition and Machine Intelligence*, vol.14301, pp.608, 2023.
- [49] H. Y. Yu, L. R. Jiang, J. L. Fan, S. Xie, R. Lan, "A Feature-Weighted Suppressed Possibilistic Fuzzy C-Means Clustering Algorithm and Its Application on Color Image Segmentation", Expert Systems with Applications, pp.122270, 2023.
- [50] K. G. Dhal, A. Das, B. Sasmal, S. Ray, R. Rai, A. Garai, "Fuzzy C-Means for image segmentation: challenges and solutions", *Multimedia Tools and Applications*, 2023.
- [51] J. X. Wu, X. P. Wang, T. Y. Wei, C. Fang, "Full-parameter adaptive fuzzy clustering for noise image segmentation based on non-local and local spatial information", Computer Vision and Image Understanding, pp.103765, 2023.
- [52] L. Madrid-Herrera, M. I. Chacon-Murguia, J. A. Ramirez-Quintana, "AENCIC: a method to estimate the number of clusters based on image complexity to be used in fuzzy clustering algorithms for image segmentation", Soft Computing, 2023.
- [53] F. Zhao, Z. H. Tang, H. Q. Liu, Z. L. Xiao, J. L. Fan, "A Reliable Region Information Driven Kriging-Assisted Multiobjective Rough Fuzzy Clustering Algorithm for Color Image Segmentation", *Expert Systems with Applications*, pp.120419, 2023.
- [54] F. Zhao, Z. L. Xiao, H. Q. Liu, Z. H. Tang, J. L. Fan, "A knee point driven Kriging-assisted multi-objective robust fuzzy clustering algorithm for image segmentation", *Knowledge-Based Systems*, vol.271, pp.110522, 2023
- [55] T. Y. Wei, X. P. Wang, J. X. Wu, S. Y. Zhu, "Interval type-2 possibilistic fuzzy clustering noisy image segmentation algorithm with adaptive spatial constraints and local feature weighting & clustering weighting", *International Journal of Approximate Reasoning*, vol. 157, pp. 1-32, 2023
- [56] Bose, A., Maulik, U., & Sarkar, A. (2024). An entropy-based membership approach on type-II fuzzy set (EMT2FCM) for biomedical image segmentation. *Engineering Applications of Artificial Intelligence*, 127, 107267.
- [57] Y. N. Pu, J. Sun, N. S. Tang and Z. B. Xu, "Deep expectation-maximization network for unsupervised image segmentation and clustering," in *Image and Vision Computing*, vol. 135, pp. 104717, Jul. 2023.
- [58] M. C. Xu, Y. K. Zhou, C. Jin, M. D. Groot, D. C. Alexander, N. P. Oxtoby, Y. P. Hu and J. Jacob, "Expectation maximization pseudo labels," in *Medical Image Analysis*, vol. 94, pp. 103125, May. 2024.
- [59] Tounsi, M., & Zitouni, M. (2024). Brain MR image segmentation for tumor detection based on Riesz probability distributions. Computer Methods in Biomechanics and Biomedical Engineering: Imaging & Visualization, 12(1), 2343711.
- [60] F. Mutlu, S. Gul, "Improving the performance of EM and K-means algorithms for breast lesion segmentation", *Anatolian Current Medical Journal*, vol.5, no.4, pp.492, 2023.
- [61] Y. Li, Y. Xuan, Q.H. Zhao, "Remote sensing image segmentation by combining manifold projection and persistent homology", *Measurement*, vol.198, pp.111414, 2022.
- [62] Alaya, B., and Sellami, L. Knowledge-based system and expectation-maximization to discovering causes of imperfect labels in vehicular networks clustering. *Knowledge-Based Systems*, 296, 111910, 2024.
- [63] U. S. Khan, Z. Liu, F. Xu, M. U. Khan, L. Chen, T. A. Khan, M. K. Khattak, and Y. Q. Zhang. "Unsupervised Color Segmentation with Reconstructed Spatial Weighted Gaussian Mixture Model and Random Color Histogram." Computers, Materials & Continua 78, no. 3 (2024).
- [64] Prabhu, V., Kuppusamy, P. G., Karthikeyan, A., & Varatharajan, R. (2018). Evaluation and analysis of data driven in expectation maximization segmentation through various initialization techniques in medical images. *Multimedia Tools and Applications*, 77(8), 10375-10390.
- [65] Zhang, X., Yin, X., Gao, X., Qiu, T., Wang, L., Yu, G., ... & Li, J. (2024).
 Adaptive Entropy Multi-modal Fusion for Nighttime Lane

- Segmentation. IEEE Transactions on Intelligent Vehicles. doi 10.1109/TIV.2024.3392413.
- [66] Maréchal, P., Navarrete, Y., & Davis, S. (2024). On the foundations of the maximum entropy principle using Fenchel duality for Shannon and Tsallis entropies. *Physica Scripta*, 99(7), 075265.
- [67] Mahajan, S., Mittal, N., Salgotra, R., Masud, M., Alhumyani, H. A., & Pandit, A. K. (2022). An efficient adaptive salp swarm algorithm using type II fuzzy entropy for multilevel thresholding image segmentation. Computational and Mathematical Methods in Medicine, 2022(1), 2794326.
- [68] M. S. A. Qaid, S. N. Basah, H. Yazid, M. H. M. Som, K. S. Basaruddin and M. K. A. Hassan, Performance analysis of diabetic retinopathy detection using fuzzy entropy multi-level thresholding. *Measurement*, 216, 112887, 2023.
- [69] E. Avci and D. Avci, "An expert system based on fuzzy entropy for automatic threshold selection in image processing," in *Expert Systems with Applications*, vol. 36, no. 2, pp. 3077-3085, Mar. 2009.
- [70] Z. W. Ye, M. W. Wang, W. Liu and S. B. Chen, "Fuzzy entropy based optimal thresholding using bat algorithm," in *Applied Soft Computing*, vol. 31, pp. 381-395, Jun. 2015.
- [71] L. Esmaeili, S. J. Mousavirad and A. Shahidinejad, "An efficient method to minimize cross-entropy for selecting multi-level threshold values using an improved human mental search algorithm," in *Expert Systems with Applications*, vol. 182, pp. 115106, Nov. 2021.
- [72] Y. Y. Jiang, D. Zhang, W. C. Zhu and L. Wang, "Multi-level thresholding image segmentation based on improved slime mould algorithm and symmetric cross-entropy," in *Entropy*, vol. 25, no. 1, pp. 178, Jau. 2023.
- [73] Q. X. Liu, N. Li, H. M. Jia, Q. Qi and L. Abualigah, "A chimp-inspired remora optimization algorithm for multilevel thresholding image segmentation using cross entropy," in *Artificial Intelligence Review*, vol. 56, pp. 159-216, Jun. 2023.
- [74] Yin, P. Y. (2007). Multilevel minimum cross entropy threshold selection based on particle swarm optimization. Applied mathematics and computation, 184(2), 503-513.
- [75] Casas-Ordaz, A., Aranguren, I., Oliva, D., Mousavirad, S. J., and Pérez-Cisneros, M. Enhancing image thresholding segmentation with a novel hybrid battle royale optimization algorithm. *Multimedia Tools and Applications*, 1-65, 2024.
- [76] Guo, H., Wang, J. G., and Liu, Y. Multi-threshold image segmentation algorithm based on Aquila optimization. *The Visual Computer*, 40(4), 2905-2932, 2024.
- [77] Khosla, T., & Verma, O. P. Optimal threshold selection for segmentation of Chest X-Ray images using opposition-based swarm-inspired algorithm for diagnosis of pneumonia. *Multimedia Tools and Applications*, 83(9), 27089-27119, 2024.
- [78] A. D. Brink and N. E. Pendock, "Minimum cross-entropy threshold selection," in *Pattern recognition*, vol. 29, no. 1, pp. 179-188, Jan. 1996.
- [79] Sahoo, P., Carrye W., and Jerry Y. "Threshold selection using Renyi's entropy." *Pattern recognition*, vol. 30, no. 1: 71-84, 1997.
- [80] P. K. Sahoo and G. Arora. "A thresholding method based on twodimensional Renyi's entropy." *Pattern Recognition*, vol. 37, no. 6: 1149-1161, 2004.
- [81] P. Kandhway, A novel adaptive contextual information-based 2D-histogram for image thresholding. Expert Systems with Applications, 238, 122026, 2024.
- [82] Mittal, H., & Saraswat, M. An optimum multi-level image thresholding segmentation using non-local means 2D histogram and exponential Kbest gravitational search algorithm. *Engineering Applications of Artificial Intelligence*, 71, 226-235, 2018.
- [83] L. Bo, L. H. He, and Z. Yang. "An efficient adaptive multilevel Renyi entropy thresholding method based on the energy curve with dynamic programming." *Soft Computing*, pp. 1-20, 2024.
- [84] Hao, S., Huang, C., Heidari, A. A., Shao, Q., & Chen, H. (2024).
 Performance optimization of hunger games search for multi-threshold COVID-19 image segmentation. *Multimedia Tools and Applications*, 83(8), 24005-24044.
- [85] Wei, L., Wang, D., & Wang, Y. (2025). Generalized relative entropy: New look at Rényi entropy and its exploration from complexity measures to sparsity measures with applications in machine condition monitoring. Mechanical Systems and Signal Processing, 223, 111917.
- [86] Chen, J., Cai, Z., Chen, H., Chen, X., Escorcia-Gutierrez, J., Mansour, R. F., & Ragab, M. (2023). Renal pathology images segmentation based on improved cuckoo search with diffusion mechanism and adaptive beta-hill climbing. *Journal of Bionic Engineering*, 20(5), 2240-2275.

- [87] S. X. Wang and J. L. Fan. "Simplified expression and recursive algorithm of multi-threshold Tsallis entropy." *Expert Systems with Applications* vol. 237, 121690, 2024.
- [88] S. X. Wang and J. L. Fan. "Image thresholding method based on Tsallis entropy correlation." *Multimedia Tools and Applications* (2024): 1-37.
- [89] Raja, N.S.M., Fernandes, S.L., Dey, N., Satapathy, S.C. and Rajinikanth, V., Contrast enhanced medical MRI evaluation using Tsallis entropy and region growing segmentation. *Journal of Ambient Intelligence and Humanized Computing*, pp.1-12, 2024.
- [90] Song, H., Wang, J., Bei, J., & Wang, M. (2024). Modified snake optimizer based multi-level thresholding for color image segmentation of agricultural diseases. Expert Systems with Applications, 255, 124624.
- [91] Guo, H., Li, M., Liu, H., Chen, X., Cheng, Z., Li, X., ... & He, Q. (2024). Multi-threshold Image Segmentation based on an improved Salp Swarm Algorithm: Case study of breast cancer pathology images. *Computers in Biology and Medicine*, 168, 107769.
- [92] Rahkar Farshi, T., & Demirci, R. (2021). Multilevel image thresholding with multimodal optimization. *Multimedia Tools and Applications*, 80(10), 15273-15289.
- [93] Lan, L., & Wang, S. (2024). Improved African vultures optimization algorithm for medical image segmentation. *Multimedia Tools and Applications*, 83(15), 45241-45290.
- [94] Lei, B., Li, J., Wang, N., & Yu, H. (2024). An efficient adaptive Masi entropy multilevel thresholding algorithm based on dynamic programming. *Journal of Visual Communication and Image Representation*, 98, 104008.
- [95] Dutta, T., Dey, S., Bhattacharyya, S., & Mukhopadhyay, S. (2021). Quantum fractional order darwinian particle swarm optimization for hyperspectral multi-level image thresholding. *Applied Soft Computing*, 113, 107976.
- [96] Samantaray, L., Tripathy, T. T., & Panda, R. (2025). A novel 3D differential entropy-based multi-class segmentation technique for brain MR image analysis. *Biomedical Signal Processing and Control*, 100, 107064.
- [97] Choudhury, P., & Boruah, B. R. (2024). Adaptive image thresholding and localization of point spread functions with enhanced precision for single molecule localization based super-resolution microscopy. *Optics and Lasers in Engineering*, 178, 108234.
- [98] Jena, B., Naik, M. K., Panda, R., & Abraham, A. (2024). Exponential entropy-based multilevel thresholding using enhanced barnacle mating optimization. *Multimedia Tools and Applications*, 83(1), 449-502.
- [99] Chen, X., Liu, C., Xie, D., & Miao, D. (2024). Image thresholding segmentation method based on adaptive granulation and reciprocal rough entropy. *Information Sciences*, vol. 695,121737.
- [100] Das, G., Swain, M., Panda, R., Naik, M. K., & Agrawal, S. (2023). A non-entropy-based optimal multilevel threshold selection technique for COVID-19 X-ray images using chance-based birds' intelligence. *Soft Computing*, 27(24), 18991-19011.
- [101] Z. Z. Wang, "A new approach for segmentation and quantification of cells or nanoparticles," in *IEEE Transactions on Industrial Informatics*, vol. 12, no. 3, pp. 962-971, Jun 2016.
- [102] Z. Z. Wang, "Automatic localization and segmentation of the ventricles in magnetic resonance images," in *IEEE Transactions on Circuits and Systems for Video Technology*, vol. 31, no. 2, pp. 621-631, Feb. 2021.
- [103] J. Hou, H. S. Lin, H. Q. Yuan, and M. Pelillo. "Flexible density peak clustering for real-world data." *Pattern Recognition* 156 (2024): 110772.
- [104] M. Abbas, E. Z. Adel and S. Amin, "DenMune: Density peak based clustering using mutual nearest neighbors." *Pattern Recognition* 109 (2021): 107589.
- [105] Yu, B., Dai, W., Li, S., Wu, Z., & Wang, J. (2024). A new threshold selection method for species distribution models with presence-only data: Extracting the mutation point of the P/E curve by threshold regression. *Ecology and Evolution*, 14(4), e11208.
- [106] Carlotto, M. J. (1987). Histogram analysis using a scale-space approach. IEEE Transactions on Pattern Analysis and Machine Intelligence, (1), 121-129.
- [107] Tsai, D. M. (1995). A fast thresholding selection procedure for multimodal and unimodal histograms. *Pattern recognition letters*, 16(6), 653-666.
- [108] Sezgin, M., & Sankur, B. L. (2004). Survey over image thresholding techniques and quantitative performance evaluation. *Journal of Electronic imaging*, 13(1), 146-168.

- [109] Brar, K. K., Goyal, B., Dogra, A., Mustafa, M. A., Majumdar, R., Alkhayyat, A., & Kukreja, V. (2024). Image segmentation review: Theoretical background and recent advances. *Information Fusion*, 102608.
- [110] Günen, M. A., & Atasever, U. H. (2024). Remote sensing and monitoring of water resources: A comparative study of different indices and thresholding methods. Science of The Total Environment, 926, 172117.
- [111] Ciecholewski, M. (2024). Review of Segmentation Methods for Coastline Detection in SAR Images. Archives of Computational Methods in Engineering, 31(2), 839-869.
- [112] Yang, Z., Zuo, S., Zhou, Y., He, J., & Shi, J. (2024). A Review of Document Binarization: Main Techniques, New Challenges, and Trends. *Electronics*, 13(7), 1394.
- [113] Amitrano, D., Di Martino, G., Di Simone, A., & Imperatore, P. (2024). Flood detection with SAR: A review of techniques and datasets. *Remote Sensing*, 16(4), 656.
- [114] Yuan, Q., Shi, Y., & Li, M. (2024). A Review of Computer Vision-Based Crack Detection Methods in Civil Infrastructure: Progress and Challenges. *Remote Sensing*, 16(16), 2910.
- [115] Y. Yu, C. P. Wang, Q. Fu, R. Kou, F. Y. Huang, B. X. Yang, T. T. Yang and M. L. Gao, "Techniques and challenges of image segmentation: A review," in *Electronics*, vol. 12, no. 5, pp. 1199, Mar. 2023.
- [116] S. Ghosh, N. Das, I. Das and U. Maulik, "Understanding deep learning techniques for image segmentation," in ACM computing surveys (CSUR), vol. 52, no. 4, pp. 1-35, Aug. 2019.
- [117] C. J. Chen, C. L. Zhang, J. L. Wang, D. N. Li and J. Hong, "Semantic segmentation of mechanical assembly using selective kernel convolution UNet with fully connected conditional random field," in *Measurement*, vol. 209, pp. 112499, Mar. 2023.
- [118] T. K. Moon, "The expectation-maximization algorithm," in *IEEE Signal Processing Magazine*, vol. 13, no. 6, pp. 47-60, Nov. 1996.
- [119] L. G. Weiss, "Wavelets and wideband correlation processing," in *IEEE Signal Processing Magazine*, vol. 11, no. 1, pp. 13-32, Jan. 1994.
- [120] J. Liu, H. Li and B. Himed, "On the performance of the cross-correlation detector for passive radar applications," in *Signal Processing*, vol. 113, pp. 32-37, Aug. 2015.
- [121] A. C. Gilbert, P. Indyk, M. Iwen and L. Schmidt, "Recent developments in the sparse Fourier transform: a compressed Fourier transform for big data," in *IEEE Signal Processing Magazine*, vol. 31, no. 5, pp. 91-100, Sep. 2014.
- [122] W. T. Cochran, J. W. Cooley, D. L. Favin, H. D. Helms, R. A. Kaenel, W. W. Lang, G. C. Maling, D. E. Nelson, C. M. Rader and P. D. Welch, "What is the fast Fourier transform?," in *Proceedings of the IEEE*, vol. 55, no. 10, pp. 1664-1674, Oct. 1967.
- [123] C. Stringer, T. Wang, M. Michaelos and M. Pachitariu, "Cellpose: a generalist algorithm for cellular segmentation," in *Nature Methods*, vol. 18, no. 1, pp. 100-106, Dec. 2020.
- [124] Y. Liu, Y. H. Wu, P. Wen, Y. J. Shi, Y. Qiu and M. M. Cheng, "Leveraging instance-, image- and dataset-level information for weakly supervised instance segmentation," in *IEEE Transactions on Pattern Analysis and Machine Intelligence*, vol. 44, no. 3, pp. 1415-1428, Mar. 2022
- [125] A. Kirillov, E. Mintun, N. Ravi, H. Mao, C. Rolland, L. Gustafson, T. T. Xiao, S. Whitehead, Alexander C. Berg, Wan-Yen Lo, P. Dollar, R Girshick, "Segment anything," in *Proceedings of the IEEE/CVF International Conference on Computer Vision (ICCV)*, pp. 4015-4026, 2023.
- [126] R. Radau, Y. L. Lu, K. Connelly, G. Paul, A. J. Dick and G. A. Wright, "Evaluation framework for algorithms segmenting short axis cardiac MRI," MIDAS J.-Card. MR Left Ventricle Segmentation Chall., 2009, https://www.midasjournal.org/browse/publication/658.
- [127] P. K. Pisharady, P. Vadakkepat and A. P. Loh, "Attention based detection and recognition of hand postures against complex backgrounds," in *International Journal of Computer Vision*, vol. 101, pp. 403-419, Aug. 2013.
- [128] Y. C. Shuang and Z. Z. Wang, "A novel approach for automatic and robust segmentation of the 3D liver in computed tomography images," in Measurement Science and Technology, vol. 31, no. 11, pp. 115701, Aug. 2020.
- [129] Y. H. Huang, X. Yang, L. Liu, H. Zhou, A. Chang, X. R. Zhou, R. S. Chen, J. X. Yu, J. Q. Chen, C. Y. Chen, S. J. Liu, H. Z. Chi, X. D. Hu, K. J. Yue, L. Li, V. Grau, Deng-Ping. Fan, F. J. Dong, D. Ni, "Segment anything model for medical images?," in *Medical Image Analysis*, vol. 92, pp. 103061, Feb. 2024.